Nonlinear LFT modelling for on-ground transport aircraft

J-M. Biannic[1], A. Marcos[2], D.G. Bates[3], and I. Postlethwaite[4]

[1] ONERA/DCSD, Toulouse, France. biannic@onera.fr
[2] Deimos-Space, Madrid, Spain. andres.marcos@deimos-space.com
[3] University of Leicester, UK. dgb3@leicester.ac.uk
[4] University of Leicester, UK. ixp@le.ac.uk

Abstract: In this chapter, a general nonlinear symbolic LFT modelling framework is first presented. Although the method is applicable to derive exact LFT models of complex nonlinear plants, it has been finally used here to generate a simplified LFT model of the aircraft-on-ground which is then useful for analysis and synthesis purpose. The assumptions that permitted to simplify the model are shown to be not so restrictive. An important contribution of the proposed method consists of an original approximation of the nonlinear ground forces which can be replaced by saturation-type nonlinearities. As a result, the simplified model boils down to a reduced-order LFT plant where the Δ block only contains time-varying or constant (but uncertain) parameters on the one hand, and saturation-type non-linearities on the other hand. Such a model is then very useful for applying modern analysis and synthesis techniques.

Notation:

θ_{NW}	Nose wheel angle, rad
$\Pi = [x\ y\ z]^T$	Earth-based aircraft position, m
$\Omega = [p\ q\ r]^T$	Angular velocities, rad/s
$\Xi = [\phi\ \theta\ \psi]^T$	Euler angles, rad
$F = [F_x\ F_y\ F_z]^T$	Body-axes total forces, N
$F_a = [X\ Y\ Z]^T$	Aerodynamic forces N
$M = [M_x\ M_y\ M_z]^T$	Body-axes total moments Nm
$V = [V_x\ V_y\ V_z]^T$	Velocity vector at c.g. m/s
$BT_{MLG_{L/R}}$	Braking torque R/L Main Landing Gear
ISV_{NW}	Servovalve steering control current, mA
ISV_{brk}	Servovalve braking control current, mA
N_{1c}	Engine fan speed target
$Tn_{L/R}$	Left/Right engine thrust, N
s_{ang}/c_{ang}	sine/cosine of angle ang

1 Introduction

In this chapter, the modelling framework proposed in Chapter 5 is used to develop a simplified LFT representation of the nonlinear on-ground Airbus model. An original nonlinear dynamic inversion (NDI) based identification procedure is developed in this chapter to obtain a simplified but accurate model of the highly nonlinear forces resulting from the interactions between the aircraft and the ground. The identification finally shows that the main nonlinearities of the model can be efficiently approximated by saturation-type nonlinearities. As a result, the structured matrix Δ of the proposed simplified LFT model contains some time-invariant and time-varying uncertainties on the one hand, and some saturation-like nonlinear operators on the other hand. Such a model, despite its nonlinear nature, is then easily handled by modern analysis and synthesis techniques as proposed in some following chapters of the book.

To improve the clarity of the presentation and to limit the complexity of the LFT model, our attention is mainly restricted to the development of a lateral model. However, an extension to the longitudinal modelling is also considered, from which a global (but also more complex) LFT model is easily obtained.

The chapter is organized as follows. For completeness, in section 3 the basic equations of the aircraft are shortly recalled. An exact LFT model and a first non-exact LFT model are briefly shown in section **??** 4. A significant contribution of the chapter is then developed in section 4.1 which focuses on the on-ground forces modelling. The LPV and ground forces models are then combined in section 5 where a lateral LFT model is proposed and is then evaluated in 6. Extensions to the longitudinal case are then discussed in section 7. Finally, some concluding remarks end the chapter.

2 NDI-based identification for LPV models

During the application of the previous chapter modelling approach to the on-ground airbus model, see subsequent sections, an off-line force identification method for LPV systems based on nonlinear dynamic inversion [**?**] was required to estimate the aircraft ground forces. The developed method is presented in this section.

Note that any nonlinear symbolic LFT representation (as those arising using the modelling approach from the last chapter) can be translated into a standard LPV model assuming the symbolic parameters are the scheduling parameters ρ of the LPV model, using the LFT feedback equation $\mathcal{F}_U(M, \Delta) = M_{22} + M_{21}\Delta(I - M_{11}\Delta)^{-1}M_{21}$ and arranging the result to yield the following LPV symbolic model:

$$\dot{x}_{LPV} = A(\rho)x_{LPV} + B_1(\rho)u + B_2(\rho)\nu \tag{1}$$

where everything can be known (or measured) except for the input vector ν.

The objective is to identify ν given all the above symbolic matrices ($A(\cdot)$, $B_1(\cdot)$, $B_2(\cdot)$) and measurements (ρ, x_{LPV}, u), together the state vector x_{NL} obtained from the nonlinear high-fidelity model (either by experimentation or simulation).

Assuming that $B_2(\rho)$ is a nonsingular square matrix for all values of the time-varying vector ρ, the dynamic equation (1) may be inverted as follows:

$$\hat{\nu} = B_2(\rho)^{-1} \left(\dot{x}_{LPV} - A(\rho) x_{LPV} - B_1(\rho) u \right) \tag{2}$$

which reveals that the derivative signal $\dot{x}_{LPV}$ can be fully controlled by an appropriate choice of $\hat{\nu}$. In other words, $\dot{x}_{LPV}$ represents the desired signal $\dot{x}_d$ in NDI theory, which in this case drives the identification procedure.

Parallelling classical control ideas, it can be shown that using a sufficiently large λ (e.g. a proportional gain), and known values of the nonlinear x_{NL} and LPV x_{LPV} state vectors, it is possible to set, for continuous trajectories, the LPV model states arbitrarily close to those from the nonlinear plant provided that the input $\hat{\nu}$ coincides with that of the LPV model in equation (1):

$$\dot{x}_d = \lambda \left(x_{NL} - x_{LPV} \right) \tag{3}$$

Therefore, the estimated input vector $\hat{\nu}$ is calculated as follows:

$$\hat{\nu} = B_2(\rho)^{-1} \begin{bmatrix} \lambda I & -A(\rho) & -B_1(\rho) \end{bmatrix} \begin{bmatrix} x_{NL} - x_{LPV} \\ x_{LPV} \\ u \end{bmatrix} \tag{4}$$

3 On-ground aircraft model

The nonlinear model characterizes the aircraft onground dynamics of a representative Airbus transport with two engines (see chapter 1 of this book) during on-ground rolling (*i.e.* taxi and after-touchdown). In this section, a general description is first presented and a simplified model is detailed next.

3.1 A general description

The open-loop nonlinear model can be represented by three main blocks of ODEs, see Figure 1. The equations of motion block, EoM, is generic for all aircraft (on-ground and airborne) and comprises the twelve standard aircraft degrees of freedom. The inputs are the total forces and moments (F and M) and the outputs are the linear and angular accelerations ($\dot{V}$ and $\dot{\Omega}$) and the kinematic ($\dot{\Xi}$) and navigation ($\dot{\Psi}$) derivatives of the states.

$$\begin{bmatrix} \dot{V} \\ \dot{\Omega} \\ \dot{\Xi} \\ \dot{\Psi} \end{bmatrix} = \begin{bmatrix} \frac{F}{m} - \Omega \wedge V \\ I^{-1}(M - \Omega \wedge (I.\Omega)) \\ T_{HB}.\Omega \\ T_{BE}.V \end{bmatrix} \tag{5}$$

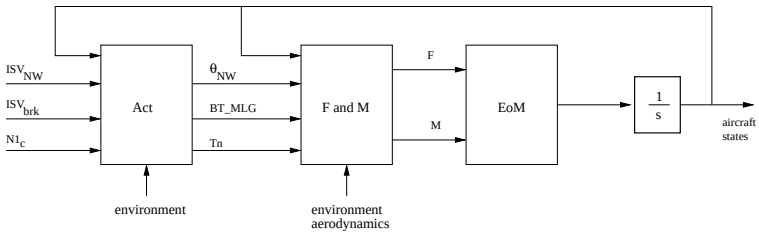

Fig. 1. On-ground aircraft model diagram

where T_{HB} and T_{BE} are transformation matrices from local-horizon to body-axes and from body-axes to Earth-frame respectively, and I is the inertial matrix. The total forces and moments FandM block has as inputs the aircraft states x, environment env and aerodynamic $aero$ data, and the actuator inputs (θ_{NW}, $BT_{MLG_{R/L}}$, $Tn_{R/L}$):

$$\begin{bmatrix} F_x \\ F_y \\ F_z \end{bmatrix} = F_a + \begin{bmatrix} -mgs_\theta \\ mgs_\phi c_\theta \\ mgc_\phi c_\theta \end{bmatrix} + \begin{bmatrix} \Sigma Tn_{R/L} \\ 0 \\ 0 \end{bmatrix} + [T_{WB}.F_w] \tag{6}$$

TWB is a transformation matrix from wheel-frame to body-frame, and F_w represents the nose wheel and landing gear contributions, which model the nonlinear interactions between the shock absorbers and the runway friction. These interactions are condensed in lateral and longitudinal forces due to wheel slip, rolling drag and braking forces (Bakker, E. and Pacejka, H.B., 1989; Barnes, A.G. and Yager, T.J, 1998; Clot, J. et al., 1998). The moments are given by, $M = FL$, where L is the proper moment-arm.

The actuator block *Act*, transforms the avionics commands from the pilot/on-ground-autopilot (ISV_{NW}, ISV_{brk} and $N1_c$) into the $FandM$ actuator inputs. This block is formed by three subsystems: nose-wheel steering system, braking system and engine model. The latter is modelled by a first quasi-steady stage followed by a dynamic model with amplitude and rate limits. The nose-wheel steering system calculates θ_{NW} using mechanical components, servovalves and pistons models for the hydraulic components:

$$\dot{\theta}_{NW} = K_1\sigma_1[ISV_{NW}]\sqrt{\frac{\sigma_2[K_2 - |\Delta P_{NW}|]}{1 + K_3\sigma_1[ISV_{NW}]}} \tag{7}$$

where σ_i represent saturation functions, Ki different NW geometric and physical constants, and ΔP_{NWS} is a nonlinear function of the pistons' pressure and θ_{NW}. Similarly for the braking system (one equation per $_{MLG}$ boggie):

$$\dot{P}_{brk} = \frac{\beta_{brk}}{V_{brk}}\eta S_{brk}[ISV_brk, P_{brk}]\sqrt{\Delta P_{brk}} \tag{8}$$

where β_{brk} is a compressibility coefficient dependent on the braking pistons' pressure difference ΔP_{brk} (which is a function of P_{brk}), V_{brk} is the piston

swept volume, η is the flow coefficient, and S_{brk} is a saturation function for the servovalve switching logic.

A set of standard on-ground manœuvres are designed to evaluate both the ground and the aerodynamic parts of the model:

- *Manœuver 1* : 40^o tiller step at T_0
- *Manœuver 2* : Doublet in tiller $20^o + 20^o$ at T_0 and $T_1 = T_0 + 10$
- *Manœuver 3* : Full acceleration until $150\,kts$ then $\pm 5^o$ doublet in pedals
- *Manœuver 4* : Idem as man.3 plus doublet of $\pm 2^o$ in tiller

3.2 Exact Nonlinear Symbolic LFT Modelling

In this section, the first three steps in the modelling approach presented in the previous chapter are used to obtain an exact nonlinear symbolic LFT model. The process is applied to each of the aircraft main blocks independently: EoM, FandM and Act blocks, but since a full and detailed presentation of the LFT modelling process is not possible, only a general view of the different steps is given for the EoM block.

Step 1 is direct in this case due to the standard manner of writing the ODEs for an aircraft motion (i.e. affine on the states or inputs).

Step 2 using the given symbolization rule yields 24 symbolic parameters (states, inertial coefficients and trigonometric functions) and no symbolic constants. Summing up the repetitions of the 24 "independent" parameters yields a value of 67.

Step 3 an *exact nonlinear symbolic LFT* of order 43 with 23 symbolic parameters is obtained. Table 1 shows the results for the three aircraft blocks using the order-reduction LFT techniques, before and after application of an additional ND numerical minimization technique [**?**] (which also keeps the exactness of the models). All the min-ND LFT models for the EoM block result in the same number of repetitions for each of the 23 parameters (not a typical situation). Thus, any of the exact min-ND LFT models models can be chosen.

Table 1. Exact LFT for EoM, FandM and Act blocks.

	EoM block		FandM block		Act block	
	no-min	**min-ND**	**no-min**	**min-ND**	**no-min**	**min-ND**
symtreed	53	43	177	134 (89)	28	26
LHT	44	43	215	180 (120)	24	24
ETD	51	43	190	139 (87)	24	24

An important consideration in applying the modelling process is to 'cover' complex function by single symbolic parameters, for example this was necessary for the on-ground forces. The example below shows how this can be performed:

Example 1. The modelling of the local sideslip angle for the wheels is shown (these are used to calculate the lateral contribution of the landing gear forces and moments):

$$\beta_{NW} = arctan\left(\frac{V_y + r\ L_{NW}}{V_x}\right) - \theta_{NW} = arctan(\tilde{\beta}_{NW}) - \theta_{NW} \tag{9}$$

$$\beta_{MLG} = arctan\left(\frac{V_y - r\ L_{MLG}}{V_x}\right) = arctan(\tilde{\beta}_{MLG}) \tag{10}$$

Choose $\rho_1 = arctan(\tilde{\beta}_{NW})$, $\rho_2 = arctan(\tilde{\beta}_{MLG})$ *and use a fictitious input to yield the exact nonlinear state-space:*

$$\begin{bmatrix} \beta_{NW} \\ \beta_{MLG} \end{bmatrix} = \begin{bmatrix} -1 & \rho_1 \\ 0 & \rho_2 \end{bmatrix} \begin{bmatrix} \theta_{NW} \\ u_f \end{bmatrix} \tag{11}$$

□

The final exact nonlinear sysmboli LFT model is obtained combining the three exact nonlinear LFTs with lowest order for each of the aircraft block. Table 2 shows the total order and the number of symbolic parameters and constants for each aircraft block –and for the "EXACT" and "NON-EXACT" (derived next) models:

Table 2. Total symbolic LFT for on-ground Airbus model: Exact and Non-exact.

	EXACT			NON-EXACT		
	order	**no.** ρ	**no.** c	**order**	**no.** ρ	**no.** c
EoM	43	24	0	8	5	2
FandM	134	27	15	41	19	10
Act	24	15	6	14	12	0
total	201	61	21	63	36	12

3.3 Non-Exact Nonlinear Symbolic LFT Modelling

In this section, Step 4 of the modelling approach from Chapter 5 is used to yield an intermediate model representing a compromise between the above exact, larger-order model and a final control-oriented, low-order model (see subsequent sections). This non-exact model facilitates the understanding and manipulations needed to obtain the final control-oriented model and also allows identifying problematic parts or non-appropriate simplifications in the case the control law designed using the most simplified model is not valid for the full nonlinear model. It is highlighted that the process is now highly automatized due to the LFT and symbolic nature of the exact LFT model –and to the use of the LFT order-reduction software.

In Chapter 1 several assumptions are taken based on the intended use of the aircraft model, i.e. design and analysis of steering and speed/braking on-ground controllers:

A.1 No inertial cross-coupling terms ($\xi_2 = \xi_4 = \xi_6 = 0 \Rightarrow$ coupling of M_x and M_z dropped).
A.2 Small-angle approximations and low speeds (less than 150 knots) $\Rightarrow$ neglect products of angles and velocity terms.
A.3 Runway is perfectly horizontal $\Rightarrow$ the lift is quasi-constant and there are almost no variations on the vertical position of the center of gravity.
A.4 Neglect compressibility effects of shock absorbers $\Rightarrow$ quasi-steady pitch and roll.
A.5 bicycle model $\Rightarrow$ superimposed left and right MLGs $\Rightarrow$ two points of contact with runway.

Assumption 4 is quite standard in the study of on-ground vehicle behavior, although for manœuvers requiring severe braking (which induces a significant pitch movement) or drastic differential thrusts (which results in rolling/yawing motion) this approximation might not be well suited. Therefore, in this first simplification model this assumption will not be considered.

Using assumptions A.1, A.2 and A.3 (interpreted as the vertical position being constant $\Rightarrow \dot{V}_z = V_z = 0$ or $F_z = 0$), the reduced **EoM** model given in equation (12) is obtained. The resulting non-exact LFT has an order of 8 for a total of 5 ρ's ($V_x,\ V_y,\ p,\ \phi,\ m^{-1}$) and 2 symbolic constants ($\xi_8 = (I_{xx} - I_{yy})/I_{zz}$, $\xi_9 = 1/I_{zz}$).

$$\begin{bmatrix} \dot{V}_x \\ \dot{V}_y \\ \dot{r} \\ \dot{\psi} \end{bmatrix} = \begin{bmatrix} 0 & V_y & m^{-1} & 0 & 0 \\ 0 & -V_x & 0 & m^{-1} & 0 \\ \xi_8 p & 0 & 0 & 0 & \xi_9 \\ \phi & 1 & 0 & 0 & 0 \end{bmatrix} \begin{bmatrix} q \\ r \\ F_x \\ F_y \\ M_z \end{bmatrix} \tag{12}$$

It is noted from the above simplification that F_z, M_x and M_y can be neglected now. Nevertheless, some of their components are required to calculate the wheel forces F_w and thus when required these terms will be directly embedded. The simplified aerodynamic F_a, M_a and engine F_{eng}, M_{eng} forces and moments in **FandM** are:

$$\begin{bmatrix} Fx_a + Fx_{eng} \\ Fy_a \\ Mz_a + Mz_{eng} \end{bmatrix} = \begin{bmatrix} S(-C_x + \alpha C_z) \\ SC_y \\ \bar{c}SC_n \end{bmatrix} [\hat{q}] + \begin{bmatrix} 1 & 1 \\ 0 & 0 \\ -Ly_{engR} & -Ly_{engL} \end{bmatrix} \begin{bmatrix} Tn_R \\ Tn_L \end{bmatrix} \tag{13}$$

where $\hat{q} = 0.5\rho_{air}V^2$, ρ_{air} is the (constant) air density, $\bar{c}$ the wing-chord, S the wing-surface and C_x, C_z, C_y, C_n are the stability-axes aerodynamic coefficients. Furthermore, using assumptions A.2 and A.3, the gravity forces can be completely neglected in this first non-exact model.

Let us now detail the forces F_w generated by the tyres friction with the ground. Using assumption A.5 these forces can be split up into nose-wheel (NW) and two, left and right, main-landing-gear (MLG) components, which after some tedious algebra yield:

$$\begin{bmatrix} Fx_w \\ Fy_w \end{bmatrix} = \begin{bmatrix} a_{11} & a_{11}atan_{NW} & -\theta \\ a_{21}|_{NW} & -a_{21}|_{NW}atan_{NW} - a_{21}|_{MLG}atan_{MLG} & \phi \end{bmatrix} \begin{bmatrix} \theta_{NW} \\ u_f \\ \bar{F}z_{NW} \end{bmatrix} + \begin{bmatrix} -1 & -\theta \\ 0 & \phi \end{bmatrix} \begin{bmatrix} \bar{F}x_{MLG} \\ \bar{F}y_{NW} \end{bmatrix} \tag{14}$$

$$a_{11} = -2s_{\theta_{NW}} G_{NW} \frac{\beta opt_{NW}^2}{\beta_{NW}^2 + \beta opt_{NW}^2} \qquad a_{21}|_{\#} = -2c_{\theta_{NW}} G_{\#} \frac{\beta opt_{\#}^2}{\beta_{\#}^2 + \beta opt_{\#}^2} \tag{15}$$

where $atan_{NW}$ and $atan_{MW}$ were defined in equations (9-10); βopt_{NW} and βopt_{MLG} correspond to optimal sideslip angles (for which maximum lateral forces are reached); and G_{NW}, G_{MLG} are referred to as the cornering gains. The yaw-moment generated by ground forces is easily obtained from the above wheel forces:

$$Mz_w = Lx_{NW}Fy_{NW} - Ly_{MLG}Fx_{MLG} + Lx_{MLG}Fy_{MLG} \tag{16}$$

Finally, applying the LFT order-reduction software a non-exact FandM LFT is obtained with an order of 41, formed by 19 symbolic parameters and 10 constants.

It is highlighted that the above representation is consistent with the mathematical tyre modelling of [**?**, **?**, **?**] where the behaviour is characterized using optimal sideslip angles and cornering gains models augmented by vertical load dependencies as illustrated in figure 2. Indeed, for small angles linear variations are expected allowing to introduce constant cornering gains. But, reality is much more complex and the determination of these gains is not that simple. In fact they will not only depend on the sideslip angles, but also on the rolling speed, vertical loads (as illustrated also in figure 2) and the runway state. The latter depends on the quality of the surface and on weather conditions (dry, wet, icy), and will induce some large variations mainly on the optimum angles βopt_{NW} and βopt_{MLG}.

After a Monte Carlo analysis of the different components for the three subsystems in the **Act** block (i.e. simulations of the ρ's from the exact LFT model of the engine, nose-wheel steering and braking subsystems), it was found that their complexity could be reduced using linear approximations based on a subset of the symbolic parameters. The NW steering system and

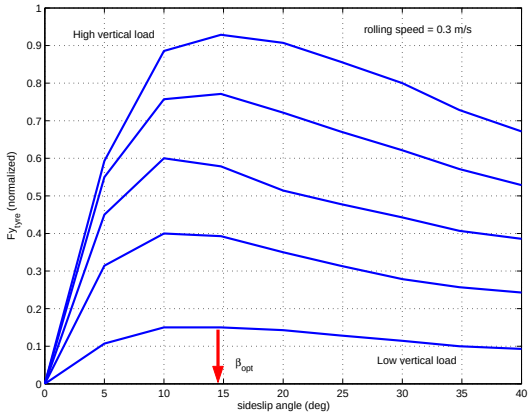

Fig. 2. Frictions forces per tyres as functions of the local sideslip angles. Dispersion with respect to vertical load F_z. Data provided by tyres manufacturers

the braking systems, one per boggie, are approximated as ($\bar{K}_i$ indicates non-symbolic constants):

$$\dot{\theta}_{NW} = \bar{K}_1 ISV_{NW} \tag{17}$$

$$\dot{P}_{brk} = \beta_{brk}(\bar{K}_2 + \bar{K}_3\sigma_1[P_{brk}] + \bar{K}_4\sigma_2[ISV_{brk}]) = \rho_1(\bar{K}_2 u_f + \bar{K}_3\rho_2 P_{brk} + \bar{K}_4\rho_3 ISV_{brk}) \tag{18}$$

where the symbolic parameters in $\dot{P}_{brk}$ represent input-normalized saturations, e.g. $\rho_2 = \frac{\sigma_1[P_{brk}]}{P_{brk}}$. Note that $P_{brk}(= \frac{1}{s}\dot{P}_{brk})$ is used to calculate the left/right braking torques $BT_{MLG} = G_{brk}P_{brk}$, see Figure **??**, where $G_{brk} = \rho_4$ is a braking disc gain with large variations. Therefore, the braking system approximation yields 8 symbolic parameters (three in $\dot{P}_{brk}$ and one –per boggie– for G_{brk}).

Finally, the engine model is (one for each wing):

$$\ddot{N}1 = LUT_1^2 N1_c - LUT_1^2 N1 - 2LUT_1 LUT_2 \dot{N}1 = \rho_9^2 N1_c - \rho_{10}^2 N1 - 2\rho_9\rho_{10}\dot{N}1 \tag{19}$$

where LUT_i are look-up tables containing the engine dynamic/static information.

Combining all the *Act* subsystems, the non-exact Act LFT model is obtained for a total of 12 symbolic parameters and a LFT order of 14. And Finally, the non-exact LFT models for each block are combined to yield the total non-exact nonlinear LFT model given in the last three columns of Table 2, which is now half the number of parameters and almost a third the order of the exact LFT model.

Figure 3 shows the time responses of the exact and non-exact LFT models using manœuver 3 from Section **??**. The responses shown are the pedal

and $N1_c$ commands (top two plots), the longitudinal velocity and its error with respect to the nonlinear model (second row), and the lateral velocity and yaw rate (bottom plot). Note that the responses of the nonlinear (solid line), exact LFT (dashed line) and non-exact LFT (dotted line) are almost indistinguishable, see the V_x error plot.

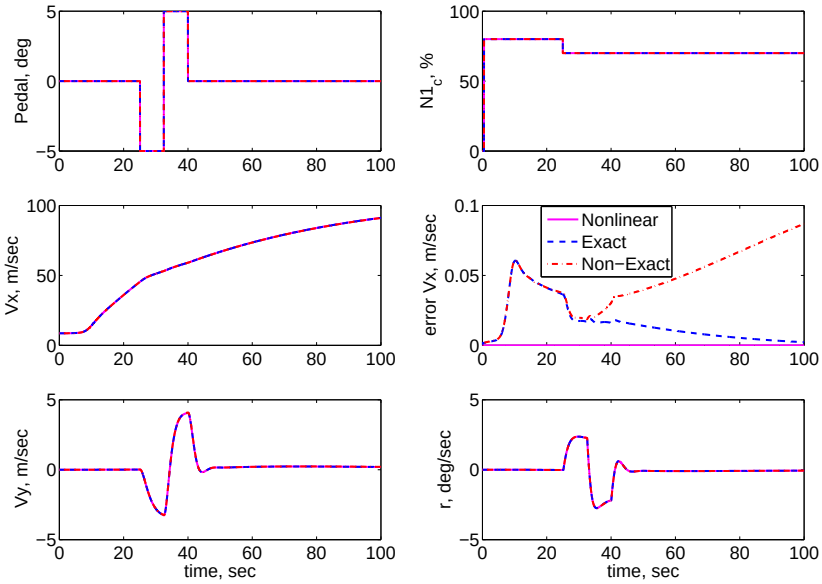

Fig. 3. Time response of nonlinear / exact LFT / non-exact LFT LFT models.

4 LPV modelling

First, it is highlighted that the focus in this work is on developing a simplified model for aircraft on-ground control design, with emphasis on the use of symmetric thrust for longitudinal control and differential thrust and nose-wheel steering for lateral/directional control. Therefore, the braking system can be neglected ($BT_{MLG} = 0$) while the engine thrusts $Tn_{R/L}$ and nose-wheel deflection θ_{NW_c} are assumed to be inputs.

Due to the last assumption, the engine models are not necessary for the control-oriented LFT model but a nose-wheel-steering system transforming θ_{NW_c} to θ_{NW} is required –based on equation (**??**). Intensive simulations have shown that, for small commanded angles, the NW-steering system behaves like a first-order linear plant whose time-constant can be approximated by

$0.1\,s$; while for higher amplitude commanded-angles, rate L_r and magnitude L_p saturations appear. Also, a small time-delay τ and a constant offset $|\theta_0| \leq 1\ deg$ on the θ_{NW} can be observed so that the NW-steering system is now described, with a very good accuracy, by :

$$\dot{\theta}_{NW}(t) = sat_{L_p}\left(\lambda\left(sat_{L_r}\left(\theta_{NW_c}(t-\tau)\right) - \left(\theta_{NW}(t) + \theta_0\right)\right)\right) \tag{20}$$

In most practical cases, the magnitude saturation is never reached, and the time-delay can be efficiently approximated by a first-order Pade function. The actuator is then further simplified as illustrated by figure 4.

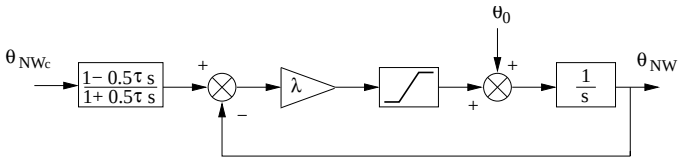

Fig. 4. Simplified Nose-wheel system.

The aerodynamic forces/moments can be simplified using assumptions A.2, simplified expressions for the aerodynamic coefficients:

$$\begin{bmatrix} Fx_a \\ Fy_a \\ Mz_a \end{bmatrix} = \frac{S\rho_{air}V_a}{2}\left(\begin{bmatrix} -Cx_0 & 0 & 0 \\ 0 & Cy_{\beta_0} & \bar{c}Cy_{r_0} \\ 0 & \bar{c}Cn_{\beta_0} & \bar{c}^2Cn_{r_0} \end{bmatrix}\begin{bmatrix} V_x \\ V_y \\ r \end{bmatrix} + \begin{bmatrix} -Cx_0 & 0 & 0 \\ 0 & Cy_{\beta_0} & V_xCy_{\delta_{r_0}} \\ 0 & Cn_{\beta_0} & V_xCn_{\delta_{r_0}} \end{bmatrix}\begin{bmatrix} W_x \\ W_y \\ \delta_r \end{bmatrix}\right) \tag{21}$$

where $C_{\#_0}$ are constants and the aerodynamic sideslip angle was approximated by $\beta_a = \frac{V_y}{V} + \frac{W_y}{V}$ with W_y denoting lateral wind (the longitudinal wind component comes from assuming only the state V_x is augmented by W_x).

The wheel forces Fx_w, Fy_w and moment Mz_w are simplified by backing up on the detailed model used in (14) and including Fy_{NW}, Fy_{MLG}, Fx_{MLG} as inputs-to-be-identified-forces that capture all the force characteristics:

$$\begin{bmatrix} Fx_w \\ Fy_w \\ Mz_w \end{bmatrix} = \begin{bmatrix} -\theta_{NW} & 1 & 0 \\ 1 & 0 & 1 \\ Lx_{NW} & -Ly_{MLG} & Lx_{MLG} \end{bmatrix}\begin{bmatrix} Fy_{NW} \\ Fx_{MLG} \\ Fy_{MLG} \end{bmatrix} \tag{22}$$

Similarly, the equations of motion were simplified to a 3-DoF model (using now assumption A.4 which implies dropping $\dot{\Psi}$ and q-contributions). Simulation with this 3DoF model, using equations (21-22) and the engine contributions from (3.3), yielded that the gravity term $Fx_g = -g\theta$ had to be added to the to V_x state in order to avoid steady-state errors. Furthermore, it was also observed that the gravity term could be approximated by $Fx_g \approx -gK_gr$ with

K_g a constant. Therefore, adding this new gravity force, we can split the almost ready LFT/LPV model $[\dot{V}_x\ \dot{V}_y\ \dot{r}]^\top$ in two parts: one fully described $[\dot{V}_{x_p}\ \dot{V}_{y_p}\ \dot{r}_p]^\top$ and another $[\dot{V}_{x_w}\ \dot{V}_{y_w}\ \dot{r}_w]^\top$ which includes the only components left to be identified Fy_{NW}, Fy_{MLG}, Fx_{MLG}:

$$\begin{bmatrix}\dot{V}_{x_p}\\ \dot{V}_{y_p}\\ \dot{r}_p\end{bmatrix} = \begin{bmatrix}-\rho_{sp}\,Cx_0\,m^{-1} & 0 & (g\,K_g + Vy)\\ 0 & \rho_{sp}\,Cy_{\beta_0}\,m^{-1} & (\rho_{sp}\,\bar{c}\,Cy_{r_0}\,m^{-1} - V_x)\\ 0 & \rho_{sp}\,\bar{c}\,Cn_{\beta_0}\,\xi_9 & \rho_{sp}\,\bar{c}^2\,Cn_{r_0}\,\xi_9\end{bmatrix}\begin{bmatrix}V_x\\ V_y\\ r\end{bmatrix}$$
$$+\begin{bmatrix}0 & m^{-1} & -\rho_{sp}\,Cx_0\,m^{-1} & 0\\ \rho_{sp}\,V_x\,Cy_{\delta_{r_0}}\,m^{-1} & 0 & 0 & \rho_{sp}\,Cy_{\beta_0}\,m^{-1}\\ \rho_{sp}\,V_x\,\bar{c}\,Cn_{\delta_{r_0}}\,\xi_9 & 0 & 0 & \rho_{sp}\,\bar{c}\,Cn_{\beta_0}\,\xi_9\end{bmatrix}\begin{bmatrix}\delta_r\\ Tn_{R/L}\\ W_x\\ W_y\end{bmatrix} \tag{23}$$

$$\begin{bmatrix}\dot{V}_{x_w}\\ \dot{V}_{y_w}\\ \dot{r}_w\end{bmatrix} = \begin{bmatrix}-\theta_{NW}m^{-1} & m^{-1} & 0\\ m^{-1} & 0 & m^{-1}\\ \xi_9 Lx_{NW} & -\xi_9 Ly_{MLG} & \xi_9 Lx_{MLG}\end{bmatrix}\begin{bmatrix}Fy_{NW}\\ Fx_{MLG}\\ Fy_{MLG}\end{bmatrix} \tag{24}$$

where the column for $Tn_{R/L}$ should be duplicated and $\rho_{sp} = 0.5S\rho_{air}V_a$.

In the remainder of the chapter the quasi-LPV model for the lateral equations will be used, the corresponging matrices are easily extracted from (23) and (24):

$$\begin{cases}\begin{bmatrix}\dot{r}\\ \dot{V}_y\end{bmatrix} = A_a(\theta)\begin{bmatrix}r\\ V_y\end{bmatrix} + B_a(\theta)\begin{bmatrix}W_y\\ \delta_r\end{bmatrix} + B_{tyres}\begin{bmatrix}F_{y_{NW}}\\ F_{y_{MG}}\end{bmatrix}\\ \begin{bmatrix}\tilde{\beta}_{NW}\\ \tilde{\beta}_{MG}\end{bmatrix} = C_\beta(\theta)\begin{bmatrix}r\\ V_y\end{bmatrix}\end{cases} \tag{25}$$

As is usual in LPV modelling, a vector θ of time-varying parameters has to be preliminarily defined. For this application the most natural choice is :

$$\theta = [V_a\ \ V_x]^T \tag{26}$$

In this model, the ground forces are represented as external inputs which have now to be further detailed. As already observed, such forces mainly depend on the sideslip angles β_{NW} and β_{MG}. From equation (**??**), the first one is easily controllable by the nose-wheel angle θ_{NW} which itself is directly controlled by the pilot through the nose-wheel system (see figure 4).

4.1 Identification of the nonlinear ground-forces

The identification of the ground forces will be exemplified using the lateral/directional components of the previous LFT/quasi-LPV model, the corresponging matrices are easily extracted from (23) and (24):

$$\begin{bmatrix} \dot{V}_y \\ \dot{r} \end{bmatrix} = A_a(V_x) \begin{bmatrix} V_y \\ r \end{bmatrix} + B_a(V_x) \begin{bmatrix} W_y \\ \delta_r \end{bmatrix} + B_{tyres} \begin{bmatrix} Fy_{NW} \\ Fy_{MLG} \end{bmatrix} \tag{27}$$

As indicated in Section 3.3, the tyre models can be shown to be composed of cornering gains G_y (dependent on vertical forces) and sideslip angles β (dependent on runway conditions $\lambda_{rwy} \in [0\,,\ 1]$ with 1 being a dry rynway with standard surface and 0 an icy one) –indices $_{NW}$ and $_{MLG}$ are omitted to alleviate the notation:

$$F_y = G_y(F_z)\beta \frac{\beta_{OPT}^2(\lambda_{rwy})}{\beta_{OPT}^2(\lambda_{rwy}) + \beta^2} \tag{28}$$

To cover all these possible variations while limiting the complexity of the model, it is proposed to consider the cornering gains as uncertain, possibly time-varying, parameters. Then, equation (28) can be rewritten as :

$$F_y = (1 + \delta_{G_y}(t)).G_{y_{nom}}.\beta.\frac{\lambda_{rwy}^2.\beta_{OPT}^2}{\lambda_{rwy}^2.\beta_{OPT}^2 + \beta^2} = (1 + \delta_{G_y}(t)).F_{y_{nom}}(\beta, \lambda_{rwy}) \tag{29}$$

The time-varying uncertain parameter satisfies $|\delta_{G_y}(t)| \leq 0.4$ which means that the precision level on the cornering gains is rather poor (40%). It should also be emphasized that the value of such gains may change also significantly from one landing to another.

Combining the lateral LPV model (27) with the lateral forces described by (29), the objective now is to compute the nominal cornering gains $G_{y_{nom}}$ and optimal sideslip angles β_{OPT} such that the outputs of the LPV model match those of the nonlinear plant. A two-step identification procedure is proposed:

- First step, using the proposed NDI-based identification approach from Section 2, a set of various lateral forces $\hat{F}_y$ is calculated for different runway conditions, rolling-speeds and external inputs so that the above objective is met,
- Second, the forces are plotted versus the corresponding sideslip angles and then the values of the cornering gains and optimal angles are obtained.

Using the on-ground manœuvres and different runway conditions, the estimated lateral forces $\hat{F}_{NW}$, $\hat{F}_{MLG}$ are plotted versus β_{NW}, β_{MLG} respectively in figure 5.

The cornering gains are first identified by bounding the plots with linear functions (as illustrated by the dashed-lines on figure 5). From these bounds extremal values of the gains are easily found, from which a mean value is immediately deduced. This is illustrated in Table 3 which also shows that the error constraints are satisfied (should be less than 40 percent).

Next we should compute the optimal values β_{OPT} of the sideslip angles β_{NW} and β_{MLG} for which the lateral forces are maximized. This is not easy task as seen in equation (29) where these parameters appear in rather complex

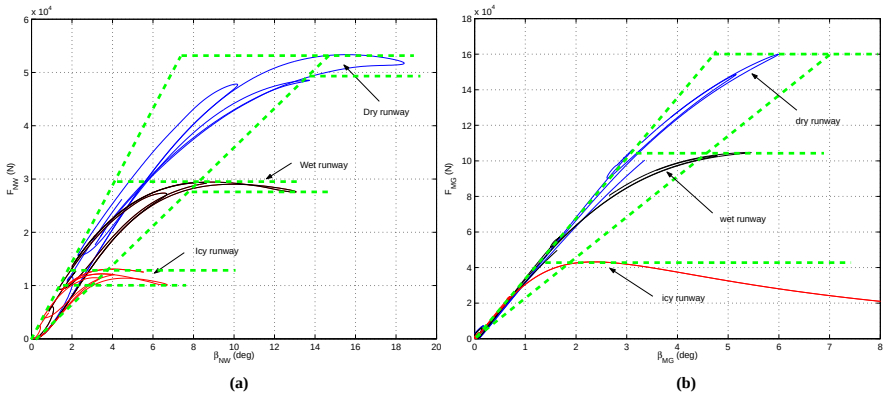

Fig. 5. (a) $\hat{F}_{NW}$ versus β_{NW} **(b)** $\hat{F}_{MLG}$ versus β_{MLG}

Table 3. Extremal and mean values of the cornering gains

	min	max	mean	error (%)
$\hat{G}_{NW}(N/rad)$	1.1 10^5	2.5 10^5	1.8 10^5	38.9
$\hat{G}_{MG}(N/rad)$	4 10^5	5 10^5	4.5 10^5	11

non-linear terms. Fortunately, from a control design and analysis perspective it is emphasized that an accurate model of the lateral forces beyond $\beta_{NW_{OPT}}$ or $\beta_{MLG_{OPT}}$ is not required. This is further supported by the fact that lateral control laws are designed so as to avoid large sideslip angles.

Introduction of saturation-type non-linearities

Based on the above remarks, an efficient simplification of the lateral ground-forces is given. As illustrated by the two plots of figure 5 (see the dashed-lines especially), the lateral forces, until β_{OPT}, are increasing functions of the sideslip angles. Thus, they can be approximated quite accurately by saturation-type nonlinearities:

$$\begin{cases} F_{y_{NW}} \approx sat_{L_{NW}(\lambda_{rwy})} \left((1 + \delta_{G_{NW}}(t)) \hat{G}_{NW}.\beta_{NW} \right) \\ F_{y_{MLG}} \approx sat_{L_{MLG}(\lambda_{rwy})} \left((1 + \delta_{G_{MLG}}(t)) \hat{G}_{MLG}.\beta_{MLG} \right) \end{cases} \tag{30}$$

where $L_{NW}(\lambda_{rwy})$ and $L_{MLG}(\lambda_{rwy})$ denote maximum lateral forces values (reached at $\beta_{NW_{OPT}}$ and $\beta_{MLG_{OPT}}$ respectively); and β_{NW}, β_{MLG} are given by equation (9-10). As shown by the two figures, these values clearly depend on the runway state λ_{rwy}. Moreover, an additional uncertainty level may be introduced on $L_{NW}(\lambda_{rwy})$ which permits to reduce the range of variations on $\hat{G}_{NW}$ (see figure 5.a).

5 LFT modelling

All the ingredients have now been introduced to complete the LFT modelling of the aircraft-on-ground. This task can be easily performed thanks to the new version of the LFR Toolbox (v2.0) [4] which can be downloaded from [5] and also with the help of additional Simulink-based tools [2] (see also [1] for a more detailed description of the tools).

5.1 Main LPV block

Using the equations (25)-(**??**), the quasi-LPV parts of the proposed model are easily converted into an LFT format. In this subsection, two LFT realization methods are evaluated. The first method is a standard numerical approach (using standard tools of the LFRT Toolbox [5], such as for example *LFRT/abcd2lfr.m*) and followed by a reduction step (*LFRT/minlfr.m*). The parameters of this LFT are: V_{x_n} (normalized version of V_x), V_{a_n} (normalized version of V_a), δ_{C_n} (LTI multiplicative uncertainty on C_n), δ_{C_y} (LTI multiplicative uncertainty on C_y).

The second method is based on a symbolic tree decomposition algorithm [3] (*LFRT/symtreed.m*) which can be applied on polynomial matrices in symbolic form (see also [6]). Therefore, following the general method of section **??** (see also [7, 8] for further details), V, V_x, $invV_x$, δ_{C_n}, δ_{C_y} are now defined as symbolic variables.

Remark: *It should be emphasized here that $invV_x$ is first considered as an independent variable. Thus, the rational expression is converted into a polynomial one. Note also at this stage that normalization is no longer necessary and even has to be avoided! This operation would indeed destroy the factorized structure of the polynomial matrix which is exploited by the algorithm to generate a low-order LFT.*

Once a reduced-order symbolic LFT is obtained, the variables V_a and V_x are rewritten as linear functions of some normalized variables V_{a_n} and V_{x_n} :

$$\begin{aligned} V_a &= \lambda_{V_a} V_{a_n} + \overline{V_a} \\ V_x &= \lambda_{V_x} V_{x_n} + \overline{V_x} \end{aligned} \tag{31}$$

where $\overline{V_a}$ and $\overline{V_x}$ denote the mean values of V_a and V_x respectively. Then, $invV_x$ is defined as the inverse of V_x. All the above elementary operations are easily achieved with the help of the overloaded *LFRT/eval.m* function. The sizes of the lateral LFTs obtained are reported in table 4.

The symbolic approach is obviously more powerful since the size of the corresponding LFT is smaller. It is worth pointing out that these two LFT, from an input/output viewpoint are equivalent. In other words, the second LFT is not an approximation of the first one. In the remainder of the chapter the reduced-size LFT will then be used. Let us denote Δ_1 the corresponding Δ-block. According to the second line of the table 4, it can be written as :

Table 4. Δ-block sizes for the LPV part of the model

	V_{a_n}	V_{x_n}	δ_{C_n}	δ_{C_r}	size of Δ_1
numerical approach	4	3	2	2	11
symbolic approach	3	3	1	1	8

$$\Delta_1 = \mathrm{diag}\,(V_n(t)I_3, V_x(t)I_3, \delta_{C_n}, \delta_{C_r}) \tag{32}$$

As illustrated by figure 6 the LFT model associated to the LPV part of the model has four inputs (W_y, δ_r, F_{NW} and F_{MG}) and four outputs ($x = [r\ V_y]^T$, β_{NW} and β_{MG}).

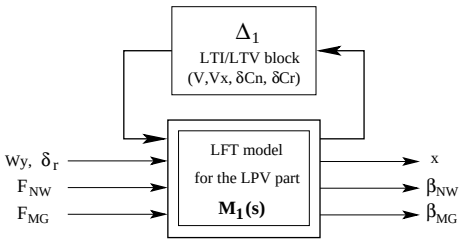

Fig. 6. LFT representation of the LPV part

5.2 Other nonlinear and LTV elements

The next step in the LFT modelling procedure is now to determine LFT models for the ground forces and for the *atan* functions which are used in the computation of the sideslip angles. LFT models for the lateral forces F_{NW} and F_{MG} are readily obtained from the equations (30). Using the function *LFRT/lfr.m*, the saturations ($sat_{L_{NW}}(.)$, $sat_{L_{MG}}(.)$) and time-varying uncertainties ($\delta_{G_{NW}}(t)$, $\delta_{G_{MG}}(t)$) are first defined as elementary LFR objects :

```
>> sat_NW = lfr('sat_NW','nlms',1);
>> sat_MG = lfr('sat_MG','nlms',1);
>> delta_NW = lfr('delta_NW','ltv',1);
>> delta_MG =  lfr('delta_MG','ltv',1);
```

then, the equations (31) are simply translated as follows :

```
>> F_NW = sat_NW*(G_NW0*(1+delta_NW))
>> F_MG = sat_MG*(G_MG0*(1+delta_MG))
```

and the global LFR object associated to the two lateral forces is finally obtained as the diagonal concatenation of *F_NW* and *F_MG*. This is achieved with the help of the overloaded *LFRT/append.m* function :

```
>> F_tyres = append(F_NW,F_MG)
```

This LFT is represented on figure 7. Its Δ-block, denoted Δ_2 is composed of two nonlinear elements (saturations) and two scalar LTV blocks associated to the uncertainties on the cornering gains :

$$\Delta_2 = \mathrm{diag}\left(\mathbf{sat}_{F_{NW}}\,,\ \mathbf{sat}_{F_{MG}}\,,\ \delta_{G_{NW}}(t)\,,\ \delta_{G_{MG}}(t)\right) \tag{33}$$

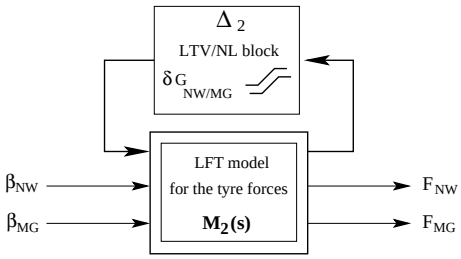

Fig. 7. LFT representation of the lateral forces

Finally, as is clear from the equations (**??**,**??**), the trigonometric *atan* functions need to be approximated. The nonlinear simulations of section 5 revealed that the sideslip angles β_{MG} at the main landing gear never exceed about $10\,deg$. Then the following approximation holds :

$$\beta_{MG} = arctan(\tilde{\beta}_{MG}) \approx \tilde{\beta}_{MG} \tag{34}$$

and only the *arctan* function associated to β_{NW} is to be considered. To cover all cases, the approximation should be valid as long as $|\tilde{\beta}_{NW}| \leq 1.2$ which corresponds to an output argument equal to 50 *deg*. As illustrated by figure 6, such an approximation (with very good precision level $< 5\%$) can be achieved by a simple piecewise affine function :

$$\begin{array}{l} |\alpha| \leq 0.4 \ \rightarrow \ f(\alpha) = \alpha \\ |\alpha| \geq 0.4 \ \rightarrow \ f(\alpha) = \frac{2}{3}\alpha + \frac{2}{15} sign(\alpha) \end{array} \tag{35}$$

which may be conveniently rewritten as follows :

$$f(\alpha) = \frac{2}{3}\alpha + \frac{2}{15}\mathbf{sat}\left(\frac{\alpha}{0.4}\right) \tag{36}$$

where **sat**(.) denotes a normalized saturation nonlinearity. As a result, the *atan* function may now be easily described by a simple LFT object (see figure 9) whose nonlinear Δ-block is a single saturation operator.

5.3 Computing the interconnection

The last phase of LFT modelling consists in connecting the above components together as illustrated by figure 10. Any linear interconnection of LFTs is well

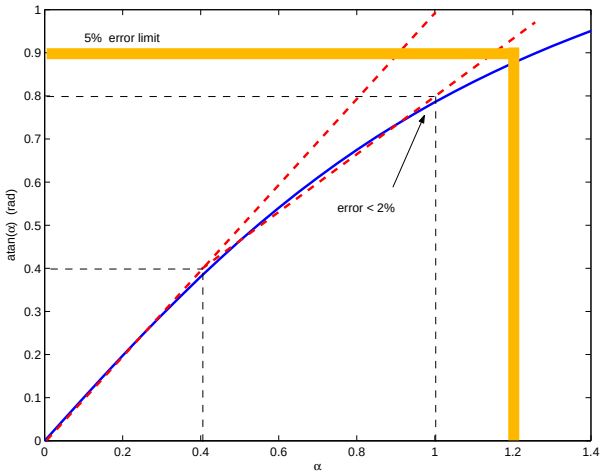

Fig. 8. Approximation of the **atan** function

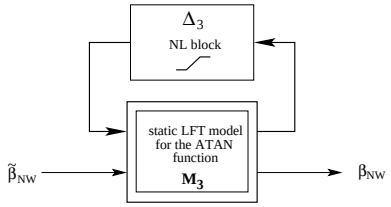

Fig. 9. LFT representation of the atan function

known indeed to be an LFT itself. This step can be performed quite easily in a Simulink environment with the help of newly developed tools [2, 1] which provide (via a specific library) a simple interface between the new version of LFR Toolbox [5] and Simulink. Using these tools, the interconnection of LFTs is simply drawn (as it appears on figure 10, but without the Δ-blocks) and saved in a Simulink file. Let us name it 'LatLFR.mdl'. Then, using a specific function *LFRT/slk/slk2lfr.m* which can be viewed as a generalization of *linmod.m*, the global LFT is readily obtained as follows :

```
>> sysLFR_LAT1 = slk2lfr('LatLFR');
```

This global LFT object has only two states and a 13×13 diagonal Δ-block which is structured as follows :

$$\Delta = diag(\Delta_{NL}, \Delta_{LTV}, \Delta_{LTI}) \tag{37}$$

with :

$$\begin{array}{l} \Delta_{NL} = diag\left(\mathbf{sat}_{atan}\,,\ \mathbf{sat}_{F_{NW}}\,,\ \mathbf{sat}_{F_{MG}}\right) \\ \Delta_{LTV} = diag\left(\delta_V(t).I_3\,,\ \delta_{V_x}(t).I_3\,,\ \delta_{G_{NW}}(t)\,,\ \delta_{G_{MG}}(t)\right) \\ \Delta_{LTI} = diag\left(\delta_{C_n}\,,\ \delta_{C_y}\right) \end{array} \tag{38}$$

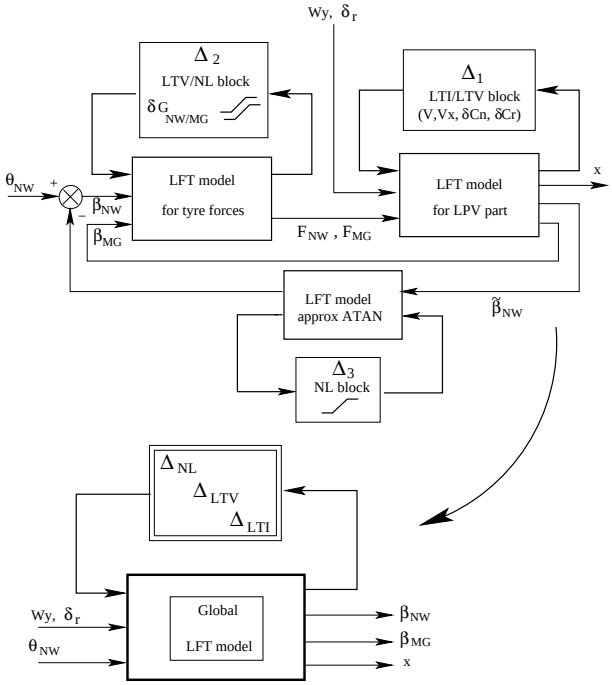

Fig. 10. LFT representation of the global interconnection

To conclude this LFT modelling, let us finally add the actuator dynamics. This is easily achieved by redrawing the Nose-wheel system of figure 4 using the LFT format as shown on figure 11.

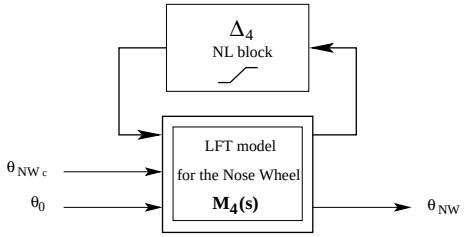

Fig. 11. LFT representation of the Nose-Wheel System

The Nose-Wheel System is then simply plugged at the third input of the interconnected LFT of figure 10. Let us denote *sysLFR_NWS* the LFR object associated to the nonlinear plant represented by figure 11. The aforementioned operation is then realized by the following command-line :

```
>> sysLFR_LAT2 = sysLFR_LAT1*append(1,1,sysLFR_NWS);
```

The newly LFR object now has three states. The LTV and LTI blocks remain unchanged, while the non-linear block is augmented :

$$\Delta_{NL} = diag\,(\mathbf{sat}_{NWS}\,,\ \mathbf{sat}_{atan}\,,\ \mathbf{sat}_{F_{NW}}\,,\ \mathbf{sat}_{F_{MG}}) \tag{39}$$

The final third-order lateral LFT model is illutrated on figure 12. Note that there are now four inputs. The first two ones are associated to the control signals while the last two can be viewed as perturbations.

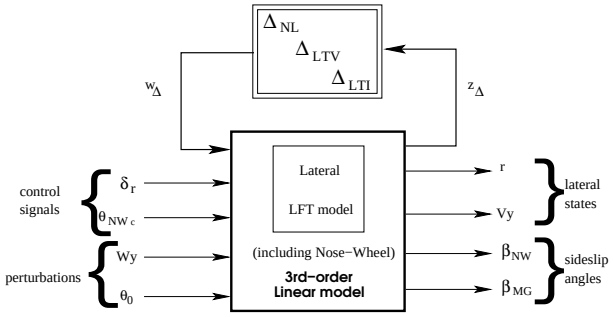

Fig. 12. LFT representation of the lateral model of the on-ground aircraft including Nose-Wheel system

6 Simulation results

Let us now compare the outputs of our simplified LFT models with those of the full nonlinear system. In these simulations, note that the longitudinal outputs of the nonlinear system (V and V_x) are directly used within the LFT model for in-line computation of the Δ-block.

In order to evaluate the accuracy of both the aerodynamic and ground models, two types of manœuvers are considered in the following tests. They correspond to the manœuvers 1 and 4 defined in the section 4.1 of this chapter. The first one is a low-speed manœuver (below $10\,kts$). High amplitude steps ($40\,deg$ for dry runway and $20\,deg$ for wet runway) are applied on the tiller. In the second manœuver, full thrust is applied on the engines until the speed exceeds $140\,kts$. During this manœuver, a small applitude ($\pm 2^o$) doublet is applied on the tiller followed by a doublet on the pedals ($\pm 5^o$).

6.1 Low-speed manœuvers

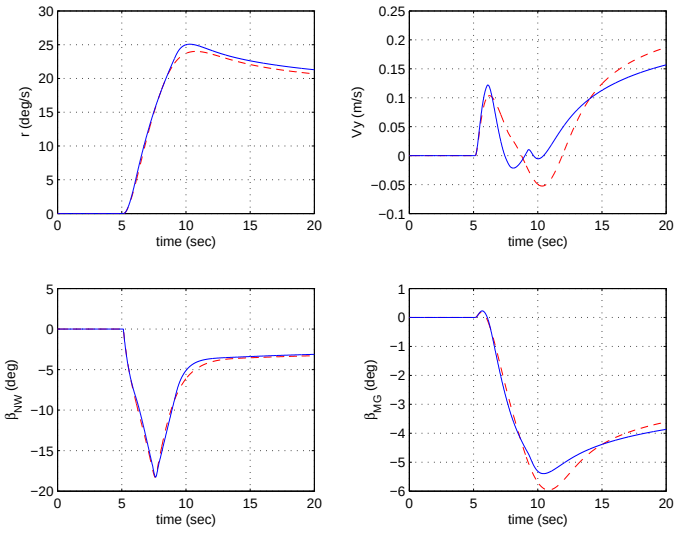

Fig. 13. Manœuver 1 : 40^o step command on tiller - Nominal runway

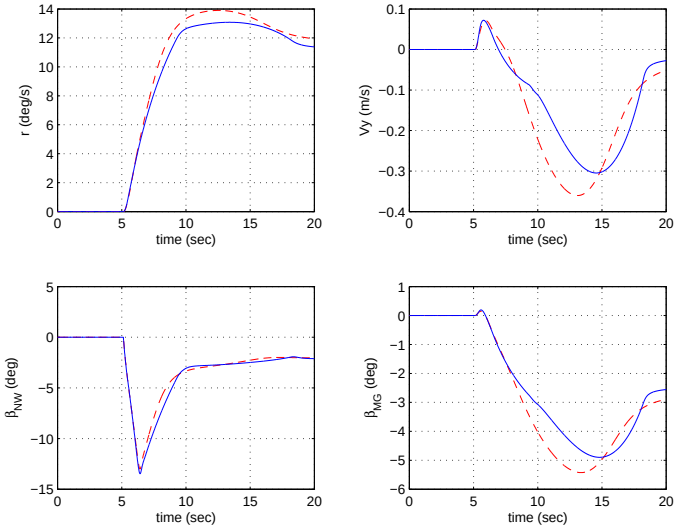

Fig. 14. Manœuver 1 : 20^o step command on tiller - Wet runway

6.2 High-speed maœeuver

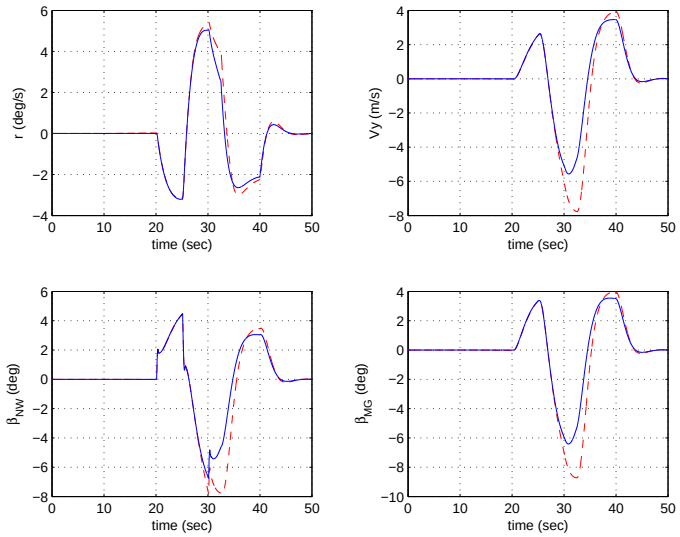

Fig. 15. Manœuver 4 : Doublet on tiller ($\pm 2^o$) followed by doublet on pedals ($\pm 5^o$)

Many more nonlinear simulations were performed to evaluate the model but are nor reported here for shortness. It appeared that, in all cases, the simplified LFT model performed well. This is especially true when only considering the yaw rate outputs (r). This means that the proposed LFT model is perfectly well-suited for the development of multivariable lateral on-ground control laws using both rudder deflection and nose-wheel control. Moreover, the proposed LFT model is also adapted for some advanced analysis tasks such as robust performance analysis in the presence of multiple saturations and lateral wind.

7 Inclusion of the longitudinal dynamics

In the above sections, we mainly focused on the lateral dynamics of the aircraft. But these are coupled with some longitudinal variables, and more specifically with V_a and V_x. Consequently, to improve the accuracy of the lateral model, but also to enable the design and analysis of longitudinal control laws, an LFT model of the longitudinal dynamics is also required. To this purpose, the same modelling procedure as for the lateral case is applicable. Let us consider first the following longitudinal equation, resulting from (5) :

$$\dot{V}_x = (r - gc_0)V_y + \frac{\rho S V}{2m} C_{x_0} (V_x - W_x) + T_n + \frac{1}{m}(F_{x_{NW}} + F_{x_{MG}}) \qquad (40)$$

where c_0 and C_{x_0} are constants obtained through simulation tests. The longitudinal ground forces at the Nose-Wheel ($F_{x_{NW}}$) are linked to the Nose-Wheel angle and the lateral forces ($F_{y_{NW}}$) :

$$F_{x_{NW}} = -\theta_{NW} F_{NW} \tag{41}$$

At the main gear, the longitudinal forces are identified by the same inversion technique which was developed for the lateral case. Here it can be observed that such forces mainly depend on the longitudinal velocity V_x. The following approximation, strongly inspired by (30) can then be proposed :

$$F_{x_{MG}} = \approx sat_{L_{x_{MG}}(\lambda_{rwy})} \left((1 + \delta_{G_{x_{MG}}}(t)) \hat{G}_{x_{MG}} . V_x \right) \tag{42}$$

From the above equations, a global LFT model is rapidly obtained. The equation (40) is first merged to the lateral LPV model (25) whose varying parameter θ has now three components:

$$\theta = [V_a \; V_x \; V_y]^T \tag{43}$$

This augmented LPV model is then rewritten in the LFT format and combined with nonlinear LFT models of the ground-forces. Note here that the equation (41) introduces an additional nonlinearity which will increase the size of the time-varying Δ-block.

$$\begin{aligned}
\Delta_{NL} &= diag \left(\mathbf{sat}_{atan} \, , \, \mathbf{sat}_{F_{x_{NW}}} \, , \, \mathbf{sat}_{F_{y_{NW}}} \, , \, \mathbf{sat}_{F_{y_{MG}}} \right) \\
\Delta_{LTV} &= diag \left(\delta_V(t) . I_3 \, , \, \delta_{V_x}(t) . I_4 \, , \, \delta_{V_y}(t) \, , \, \delta_{\theta_{NW}}(t) \, , \, \delta_{G_{y_{NW}}}(t) \, , \, \delta_{G_{y_{MG}}}(t) \right) \\
\Delta_{LTI} &= diag \left(\delta_{C_n} \, , \, \delta_{C_x} \, , \, \delta_{C_y} \right)
\end{aligned} \tag{44}$$

Let us finally check the validity of the full LFT model under high-speed conditions by considering the fourth manœuver which consists of a full acceleration until $150\,kts$ followed by doublets on the pedals and tiller. As shown on figure 16, it can be observed that the model performs very well. Note that the error on the longitudinal speed V_x, which is now a state of the full model, remains particularly small. Moreover, as in the previous cases, very small deviations are observed on the lateral variables (r and V_y) as well.

8 Conclusion

In this chapter, a complete methodology has been described to develop a simple LFT model for an aircraft-on-ground. The case of the lateral motion has received a particular attention and was then extended to take the longitudinal dynamics into account as well. Interestingly, despite its simplicity, the proposed model performs very well on a large operating domain. It will then be very useful not only for the development of new on-ground control systems as proposed in chapter 6 for example, but also for the application of robust and nonlinear analysis techniques as developed in chapters 8 and 9.

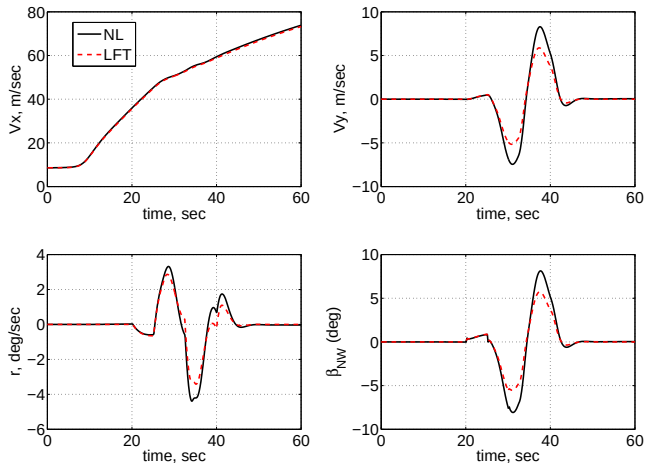

Fig. 16. Manœuver 4 : Doublet on tiller ($\pm 2^o$) followed by doublet on pedals ($\pm 5^o$) on icy runway

References

1. J-M. Biannic and C. Doll. Graphical tools for creating and simulating interconnected LFR objects. In *IEEE-CCA-CACSD Conference*, Munich, Germany, October 2006.
2. J-M. Biannic and C. Doll. Simulink handling of LFR objects. Free Web publication *http://www.cert.fr/dcsd/idco/perso/Biannic/mypage.html*, 2006.
3. J.C. Cockburn and B.G.Morton. Linear fractional representations of uncertain systems. *Automatica*, 33(7):1263–1271, 1997.
4. S. Hecker, A. Varga, and J-F. Magni. Enhanced LFR Toolbox for MATLAB. In *IEEE International symposium on computer aided control system design*, Taipei, Taiwan, September 2004.
5. J-F. Magni. Linear Fractional Representation Toolbox (version 2.0) for use with Matlab. Free Web publication *http://www.cert.fr/dcsd/idco/perso/Magni/*, 2006.
6. A. Marcos, D. G. Bates, and I. Postlethwaite. A Multivariate Polynomial Matrix Order Reduction Algorithm for Linear Fractional Transformation Modelling. In *IFAC World Congress on Automatic Control*, Pragues, July 2005.
7. A. Marcos, D. G. Bates, and I. Postlethwaite. Exact Nonlinear Modelling using Symbolic Linear Fractional Transformations. In *IFAC World Congress on Automatic Control*, Pragues, July 2005.
8. A. Marcos, J-M. Biannic, M. Jeanneau, D. G. Bates, and I. Postlethwaite. Aircraft Modelling for Nonlinear and Robust Control Design and Analysis. In *IFAC Symposium on Robust Control Design*, Toulouse, June 2006.